Single-impulse panoramic photoacoustic computed tomography of small-animal whole-body dynamics at high spatiotemporal resolution

Lei Li[1,2‡], Liren Zhu[2,3‡], Cheng Ma[3,4†‡], Li Lin[2,3‡], Junjie Yao[3†], Lidai Wang[3†], Konstantin Maslov[2], Ruiying Zhang[3], Wanyi Chen[3], Junhui Shi[2] and Lihong V. Wang[2,4*]

Imaging of small animals has played an indispensable role in preclinical research by providing high-dimensional physiological, pathological and phenotypic insights with clinical relevance. Yet, pure optical imaging suffers from either shallow penetration (up to ~1–2 mm) or a poor depth-to-resolution ratio (~3), and non-optical techniques for whole-body imaging of small animals lack either spatiotemporal resolution or functional contrast. Here, we demonstrate that stand-alone single-impulse panoramic photoacoustic computed tomography (SIP-PACT) mitigates these limitations by combining high spatiotemporal resolution (125 μm in-plane resolution, 50 μs per frame data acquisition and 50 Hz frame rate), deep penetration (48 mm cross-sectional width in vivo), anatomical, dynamical and functional contrasts, and full-view fidelity. Using SIP-PACT, we imaged in vivo whole-body dynamics of small animals in real time and obtained clear sub-organ anatomical and functional details. We tracked unlabelled circulating melanoma cells and imaged the vasculature and functional connectivity of whole rat brains. SIP-PACT holds great potential for both preclinical imaging and clinical translation.

Small animals, especially rodents, are essential models for preclinical studies, and they play an important role in modelling human physiology and development, in guiding the study of human diseases and in seeking effective treatment[1]. The ability to directly visualize dynamics with high spatiotemporal resolution in these small-animal models at the whole-body scale provides insights into biological processes at the whole-organism level[2]. In addition to high spatiotemporal resolution, the ideal non-invasive small-animal imaging technique should provide deep penetration, and anatomical and functional contrasts. Previously, small-animal whole-body imaging has typically relied on non-optical approaches, including magnetic resonance imaging (MRI), X-ray computed tomography (X-ray CT), positron emission tomography (PET) or single-photon emission computed tomography (SPECT), and ultrasound tomography (UST)[3,4]. Although these techniques provide deep penetration, they suffer from significant limitations. For example, adapting MRI to achieve microscopic resolution requires a costly high magnetic field and a long data acquisition time, ranging from seconds to minutes, which is too slow for imaging dynamics[5,6]. X-ray CT lacks functional contrast[7]. PET and SPECT alone suffer from poor spatial resolution. In addition, X-ray CT, PET and SPECT use ionising radiation, which may inhibit longitudinal monitoring[8]. UST does not image blood oxygenation or extravascular molecular contrasts[9]. To overcome all of the above limitations using one system, new imaging modalities need to be developed.

Optical imaging of biological tissue employs noncarcinogenic electromagnetic waves to provide extraordinary structural, functional and molecular contrasts with either endogenous or exogenous agents[10–12]. Unfortunately, the application of conventional optical imaging technologies to small-animal whole-body imaging is impeded by the strong optical scattering of tissue, which prevents high-resolution imaging beyond the optical diffusion limit of approximately 1–2 mm in depth[3]. Although diffusive optical imaging methods, such as fluorescence diffuse optical tomography[13], can provide centimetres of penetration, their image resolution is rather poor (approximately one-third of the depth).

To date, photoacoustic tomography (PAT) is the only high-resolution optical imaging modality that breaks the optical diffusion limit[14]. In PAT, the energy of incident photons is absorbed by chromophores inside the tissue to be imaged and re-emitted as ultrasonic waves. The ultrasonic waves are subsequently detected to generate tomographic images with optical contrasts. Owing to the weak scattering of ultrasound in soft tissue (about three orders of magnitude weaker than light scattering on a per unit path length basis in the ultrasonic frequency of interest), PAT produces superb resolution at depths, with a depth-to-resolution ratio of approximately 200 (ref. [15]). Combining the advantages of optical contrasts and acoustic detection, PAT holds great promise for a full-package solution to small-animal whole-body imaging. Currently, PAT has been implemented primarily in the forms of scanning-based photoacoustic microscopy (PAM) and reconstruction-based photoacoustic computed tomography (PACT). We have demonstrated high-speed, high-resolution functional PAM of the mouse brain in action, with penetration up to several millimetres[16]. PACT has provided penetration beyond 10 mm, but with either poor temporal resolution, due to data acquisition multiplexing[17–19], or unclearly resolved sub-organ features,

due either to partial acoustic detection coverage[20,21] or to sparse spatial sampling[22–24]. High-performance small-animal whole-body imaging requires the simultaneous integration of high spatiotemporal resolution, deep penetration, multiple contrasts, full-view fidelity and high detection sensitivity in one system.

Here, we report a significant advance in PACT technology that overcomes all of the aforementioned limitations, which are prevalent in both non-optical and pure optical imaging techniques. Our imaging technology—single-impulse panoramic PACT (SIP-PACT)—allows us to capture structural, functional, cellular and molecular small-animal whole-body images with unprecedented speed and quality. SIP-PACT employs 512-element full-ring acoustic detection with simultaneous one-to-one mapped preamplification and analogue-to-digital sampling. A single laser pulse, sufficiently short to be treated as an impulse, excites photoacoustic waves, which are detected within 50 μs for two-dimensional (2D) imaging of a cross-section. The 2D panoramic acoustic detection scheme provides 125 μm isotropic in-plane resolution within a field of view (FOV) of about 16 mm in diameter (see Methods), and full-view fidelity (for instance, no partial-view artefacts)[25]. Moreover, to better reveal detailed features inside the body, we developed a half-time dual-speed-of-sound universal back-projection (UBP) algorithm to compensate for the first-order effect of acoustic inhomogeneity. SIP-PACT enables a number of new whole-body imaging capabilities, with performance complementary to those of the aforementioned non-optical approaches. At a 50 Hz frame rate, it non-invasively images whole-body small animals (up to 48 mm in width), with sub-organ vasculature and internal organ structures clearly resolved, without any labelling. At such high spatiotemporal resolutions, the biological dynamics associated with heartbeats and respiration are clearly observed without motion artefacts. Taking advantage of the absorption spectral signatures of oxyhaemoglobin and deoxyhaemoglobin, SIP-PACT provides fast mouse brain and whole-body functional imaging. Naturally, SIP-PACT can be used to monitor live animals over a long duration for drug testing without the potentially detrimental interference of an ionising radiation overdose, such as that associated with X-ray CT use. With the assistance of a near-infrared (NIR) dye, SIP-PACT shows the process of dye perfusion in both the mouse brain and internal organs, demonstrating the capability of molecular imaging. SIP-PACT visualizes

and tracks circulating tumour cells (CTCs) in a live mouse brain without any labelling. Moreover, SIP-PACT sees through the rat whole brain (as deep as 11 mm) and detects the functional connectivity in the deep brain (up to 9.7 mm).

Results

Label-free imaging of small-animal whole-body anatomy and dynamics. For 2D panoramic in-plane acoustic detection in SIP-PACT, we used a 512-element full-ring ultrasonic transducer array with a central frequency of 5 MHz and a one-way bandwidth of more than 90% (see Supplementary Fig. 1 and Methods). This avoids artefacts induced by limited detection coverage[25]. The digitized raw data were fed into a half-time dual-speed-of-sound (in tissue and water) UBP algorithm (Supplementary Figs 2 and 3 and Methods) for image reconstruction. Two different illumination approaches were applied, respectively, for imaging the mouse brain cortex and trunk (Fig. 1, Supplementary Fig. 4 and Methods). Top illumination and side detection were used for brain cortex imaging, and full-ring side illumination and side detection (aligned confocally to maximize detection sensitivity) were used for trunk imaging. To maximize optical penetration, we took advantage of the 'optical window', 650–1,350 nm, where mammalian tissues least attenuate light. We used 1,064 nm laser excitation with a 50 Hz pulse repetition rate for this task. SIP-PACT non-invasively imaged the vasculature of the brain cortex (Fig. 2a), as well as the anatomy of the internal organs within the thoracic cavity (heart and lungs; Fig. 2b,c) and the abdominal cavity (liver, spleen, kidney, caecum and intestine; Fig. 2d–f). Detailed structures were revealed by haemoglobin contrast (Methods and Supplementary Fig. 5). As with many other tomographic imaging modalities, after scanning the animal vertically through the confocal plane and stacking the slices of cross-sectional images, we compiled a three-dimensional tomogram of the mouse trunk (Supplementary Video 1). The thickest section of the mouse trunk had a width of 28 mm (Fig. 2e,f), and the entire cross-section was clearly imaged with a spatial resolution of 125 μm (Supplementary Figs 6 and 7). At an imaging frame rate of 50 Hz, respiratory motions and heartbeats were fully captured at well above the Nyquist sampling rate (Supplementary Videos 2–6). The substantially improved system performance and whole-body image quality (Supplementary Figs 8–12 and Supplementary Video 7)
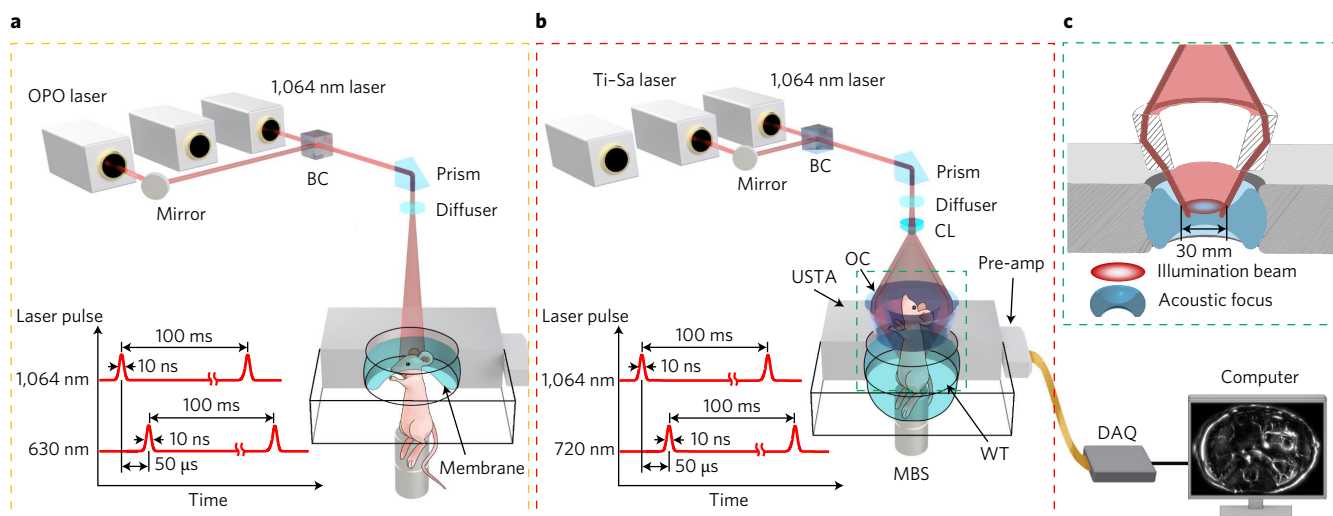
Figure 1 | Schematics of the SIP-PACT system. a,b, Brain (**a**) and trunk (**b**) imaging. During dual-wavelength illumination, all lasers fire at 10 Hz and the delay time between the dual-pulse is 50 μs. For single-wavelength illumination, the 1,064 nm laser fires at 50 Hz and the Ti:Sapphire (Ti–Sa) laser fires at 20 Hz. **c**, Close up of the green dashed box region in **b**, which shows the confocal design of light delivery and photoacoustic wave detection. BC, beam combiner; CL, conical lens; DAQ, data acquisition system; MBS, magnetic base scanner; OC, optical condenser; OPO, optical parametric oscillator; USTA, (full-ring) ultrasonic transducer array; WT, water tank.

enable SIP-PACT to complement other small-animal whole-body anatomical imaging modalities.

In one cross-sectional image of the thoracic cavity (Figs 2b and 3a), both respiratory motion and heartbeats are displayed (Supplementary Video 2). By recording the signal changes of a rib (along the red solid line in Fig. 3a) and the heart wall (along the blue dashed line in Fig. 3a), the respiratory motion and heartbeats can be tracked and identified (Fig. 3b). Fourier analysis shows that the motion of the rib repeated at a respiratory frequency of around 1 Hz, and that the motion of the heart wall repeated at both the respiratory frequency and a heartbeat frequency of around 5.2 Hz (Fig. 3c and Supplementary Figs 13 and 14).

Within a cross-sectional view of the lower abdominal cavity (Supplementary Video 6), the signals from arteries are temporally correlated due to their direct connection to the heart. The high imaging speed and the single-impulse acquisition capability of SIP-PACT enabled us to selectively map the arterial network on the whole-body cross-sectional image. By pixel-wise calculation of the amplitude at the heartbeat frequency (see Methods), the arterial network can be mapped on the whole-body cross-sectional image (Fig. 3d), where the renal arterial network of the right kidney is highlighted by heartbeat encoding. During systole, the aortic wall dilates due to the ejection of blood from the contracted left ventricle, generating a pressure wave that travels along the arterial tree. We selected two vertically distributed arteries from the arterial network (highlighted by arrows 1 and 2 in Fig. 3d) to compute the changes of the cross-sectional areas (Fig. 3e and Supplementary Video 8). A steady phase delay
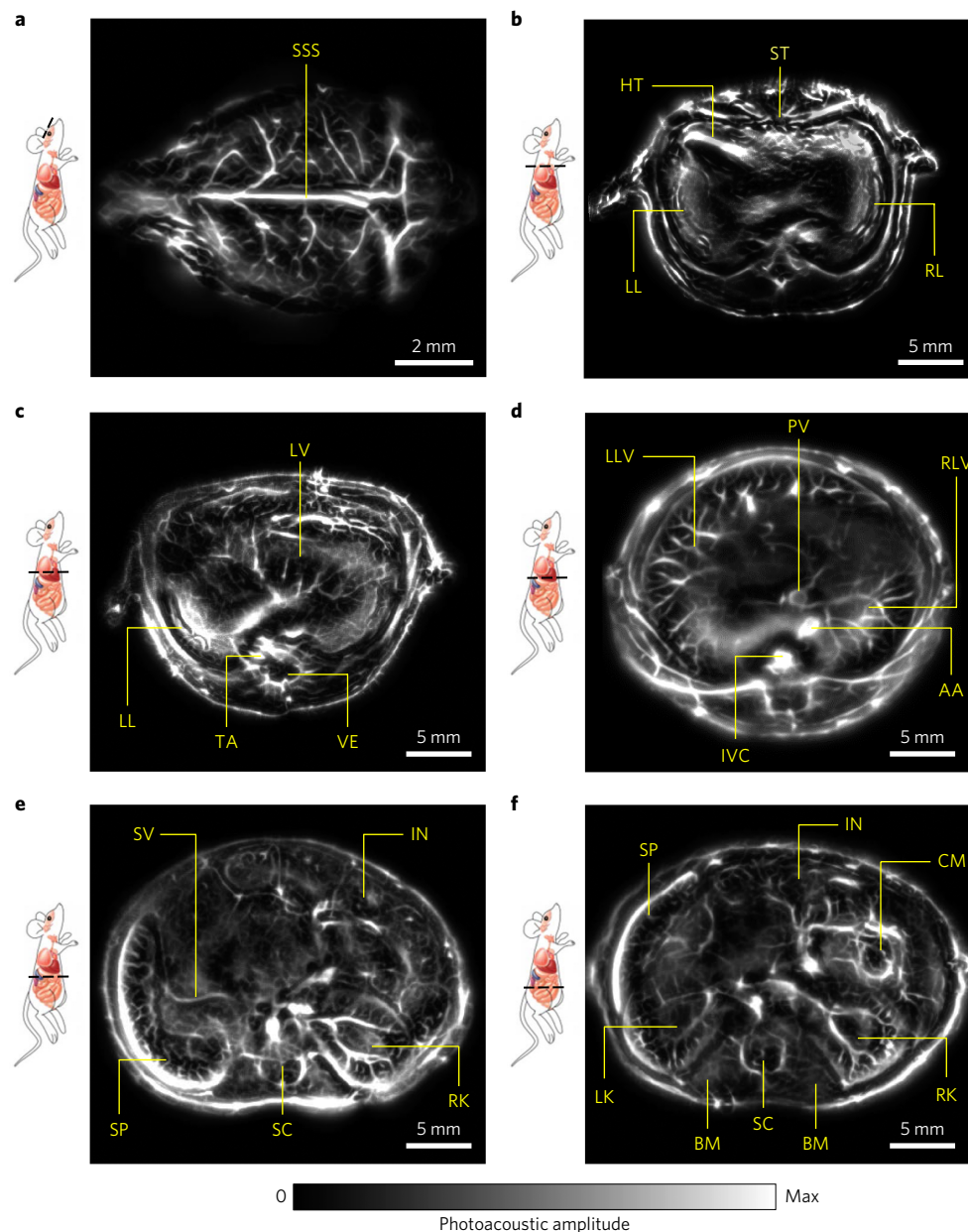
Figure 2 | Label-free SIP-PACT of small-animal whole-body anatomy from the brain to the trunk. a, Vasculature of the brain cortex. **b–f**, Cross-sectional images of the upper thoracic cavity (**b**; Supplementary Video 2), lower thoracic cavity (**c**; Supplementary Video 3), two lobes of the liver (**d**; Supplementary Video 4), upper abdominal cavity (**e**; Supplementary Video 5) and lower abdominal cavity (**f**; Supplementary Video 6). AA, abdominal aorta; BM, backbone muscles; CM, caecum; HT, heart; IN, intestines; IVC, inferior vena cava; LK, left kidney; LL, left lung; LLV, left lobe of liver; LV, liver; PV, portal vein; RK, right kidney; RL, right lung; RLV, right lobe of liver; SC, spinal cord; SP, spleen; SSS, superior sagittal sinus; ST, sternum; SV, splenic vein; TA, thoracic aorta; VE, vertebra.
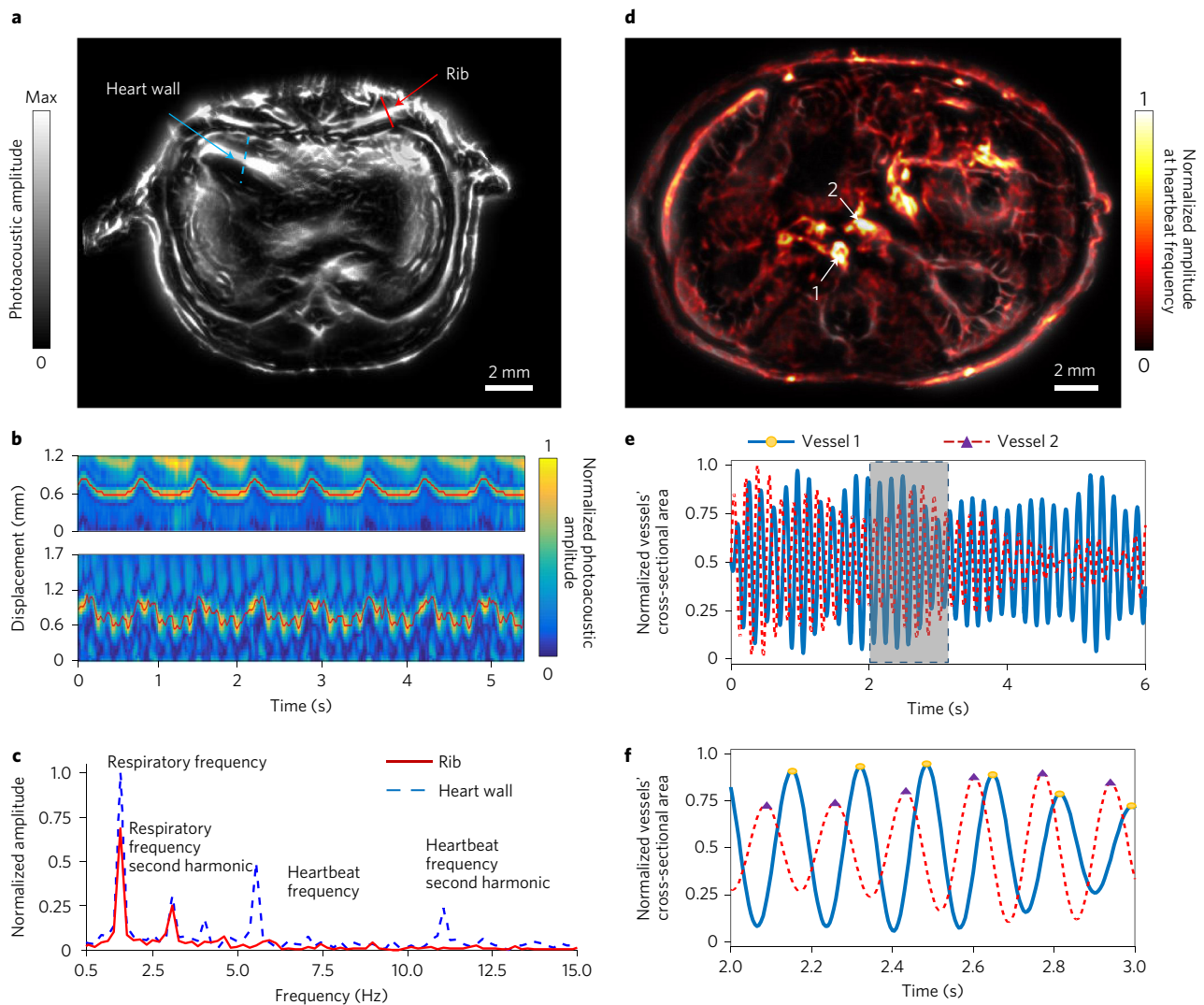
Figure 3 | Label-free imaging of small-animal whole-body dynamics. a, Cross-sectional image of the upper thoracic cavity, where the red solid line crosses a rib, and the blue dashed line crosses the heart wall. **b**, Line profiles in **a** versus time show the displacements of the rib (upper panel) during respiration and the heart wall (lower panel) during heartbeats. The traces of the rib and heart wall movements are identified and highlighted with solid red lines. **c**, Fourier transforms of the rib and heart wall movements showing the respiratory frequency and heartbeat frequency, respectively. **d**, Heartbeat encoded arterial network mapping overlaid on the anatomical image. **e**, Cross-sections of the vessels highlighted by the arrows in **d**, showing changes associated with arterial pulse propagation (Supplementary Video 8). **f**, Enlargement of the dashed box in **e**, showing the relative phase delay between the two curves of the vessels' cross-sections.

is revealed in the close-up panel (Fig. 3f), indicating that the changes of the cross-sectional areas are the result of the pulse wave propagating through the arterial network. This demonstrates that SIP-PACT can non-invasively map the whole-body arterial network and measure the relative pulse wave phase difference between arteries. This capability could provide a non-invasive and direct diagnostic tool for chronic coronary artery disease and chronic renal disease[26,27].

SIP-PACT of whole-body oxygenation dynamics. By taking advantage of the difference between the oxy- and deoxyhaemoglobin absorption spectra, we can image whole-body oxygenation dynamics by exciting photoacoustic waves alternately with two optimal wavelengths. To systemically modulate the oxygen saturation of haemoglobin (sO_2), we manipulated the oxygen concentration in the inhalation gas.

By illuminating the mouse brain from the top (Fig. 1a) with two laser pulses of different wavelengths at a biologically negligible delay

($50\,\mu s$), we non-invasively imaged both the cortical vasculature and the sO_2 of the cortical vessels *in vivo* (Fig. 4a,b, Supplementary Video 9 and Methods). In this experiment, a mixture of 95% oxygen and 5% nitrogen was initially used with gaseous isoflurane for anaesthesia. During the oxygen challenge, the mixture was switched to 5% oxygen and 95% nitrogen for 3 min (4.5 min for whole-body oxygen challenge), and then switched back to the initial concentration to end the challenge. We estimated the systemic sO_2 change by averaging signals over the superior sagittal sinus—the central vessel shown in colour in Fig. 4a,b. Variations in sO_2 (Fig. 4c), derived from changes in oxy- and deoxyhaemoglobin concentrations (Fig. 4d), were observed following the manipulation of the inhalation oxygen concentration. The sO_2 drop resulting from hypoxia is manifestly slower than its recovery, consistent with previous observations[28,29].

Blood-oxygen-level-dependent (BOLD) MRI, which is widely used for functional studies in both animal models and humans, is sensitive primarily to the concentration of deoxyhaemoglobin[30,31]. Similar to BOLD MRI, SIP-PACT can also map the trunk's
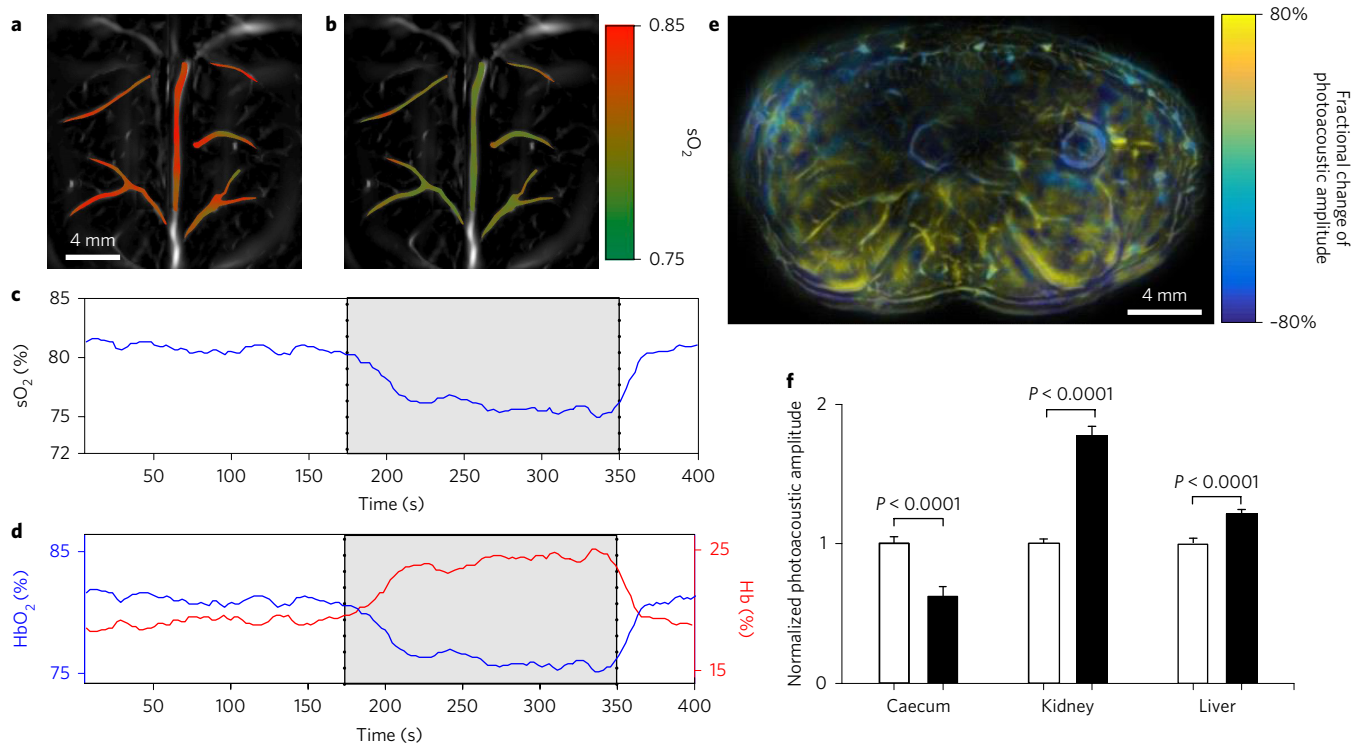
Figure 4 | SIP-PACT of mouse whole-body oxygenation dynamics. a,b, sO_2 mapping of mouse cortical vasculatures during hyperoxia (**a**) and hypoxia (**b**). **c**, Brain sO_2 changes during oxygen challenges. The grey rectangle outlines the challenge periods (Supplementary Video 9). **d**, Changes in the concentrations of oxyhaemoglobin (HbO_2) and deoxyhaemoglobin (Hb) during oxygen challenges. The grey rectangle outlines the challenge periods. **e**, Fractional changes in the blood oxygen level in the cross-sectional image of the lower abdominal cavity (Supplementary Video 10). **f**, Normalized photoacoustic amplitude, corresponding to blood oxygen level, in internal organs during hyperoxia and hypoxia, where the hollow bars represent the baseline amplitudes and the solid bars represent the plateau amplitudes during challenge ($n = 50$, error bars are s.e.m.). The P-values were calculated using a paired Student's t-test. See Methods for details.

haemodynamic response to a change in oxygen supply by using a single deoxyhaemoglobin-sensitive wavelength for excitation, but at a higher imaging speed and greater sensitivity than those of BOLD MRI (Supplementary Fig. 15a,b and Methods). After we switched the oxygen concentration from 95% to 5%, the whole-body oxygenation levels changed accordingly (Fig. 4e and Supplementary Video 10). Since deoxyhaemoglobin has a much stronger molar optical absorption than oxyhaemoglobin at the excitation wavelength of 720 nm, the photoacoustic signal changes mainly reflected the whole-body deoxyhaemoglobin concentration changes. In Fig. 4e, yellow represents a positive relative photoacoustic signal change, which means a decrease in sO_2, while blue shows a negative relative photoacoustic signal change, meaning that sO_2 increased. When a global shortage of oxygen occurs, the whole-body sO_2 should drop accordingly. We observed a relative sO_2 decrease in most of the organs, such as the brain, liver and kidney, and an sO_2 increase in some organs, such as the caecum (Fig. 4f; Supplementary Fig. 15c,d). These observations might be explained as follows. Once global hypoxia occurs, the animal adjusts its whole-body metabolic activity to survive the challenge. The vital organs, such as the brain, heart and kidney, must maintain their basic functions with normal metabolic activities, so their maintained oxygen consumption under hypoxia leads to an sO_2 drop[32]. As some other organs, such as the caecum, reduce their metabolic activity to save oxygen for other vital organs, a reduced oxygen extraction fraction leads to an sO_2 increase within those organs[33–35]. For the first time, to our knowledge, we have photoacoustically imaged the dynamics of whole-body oxygenation distribution across internal organs with great detail *in vivo* and without labelling.

Label-free tracking of CTCs in the mouse brain *in vivo*. CTCs have been regarded as an important pathway and a potential indicator for tumour metastasis, a hallmark of tumour malignancy[36,37]. Tracking the fate of metastasising cancer cells *in vivo* is vitally important to the study of early extravasation, early angiogenesis and the treatment of cancer[38]. In this study, we targeted melanoma, a skin cancer which was expected to cause an estimated 10,130 fatalities in the United States in 2016[39], and demonstrate that our SIP-PACT system is capable of *in vivo* monitoring of melanoma migration in the entire mouse cortical vasculature. Melanin has a much stronger optical absorption, at around 680 nm, than haemoglobin (Supplementary Fig. 16). Hence, we used SIP-PACT with 680 nm laser excitation to capture the migration of intra-arterially injected melanoma cancer cells along cortical vessels (Supplementary Video 11 and Methods) in real time, with high contrast and without any labelling. It should be noted that the injected melanoma cells could present in the bloodstream in the form of both single cells and CTC clusters, contributing to the strong signals in our images. A motion-contrast image was created (see Methods) from signals before (Fig. 5a) and after CTC injection and overlaid on the vascular image. This shows the melanoma cancer cells (Fig. 5b), where colours represent the flow directions of CTCs. The movements of melanoma cancer cells in the yellow dashed box region in Fig. 5a are visualized in Fig. 5c, where the melanoma cells in the current frame are highlighted in red, their initial positions are shown by yellow crosses and the flow path of each cell is marked by an orange dashed line. By tracking the melanoma cells in real time and analysing the movement of flowing melanoma cells in the spatiotemporal frequency domain (see Methods), we can compute the flow rate of the cancer cells, which is slower that of the cerebral blood[40,41]. We extracted the time traces
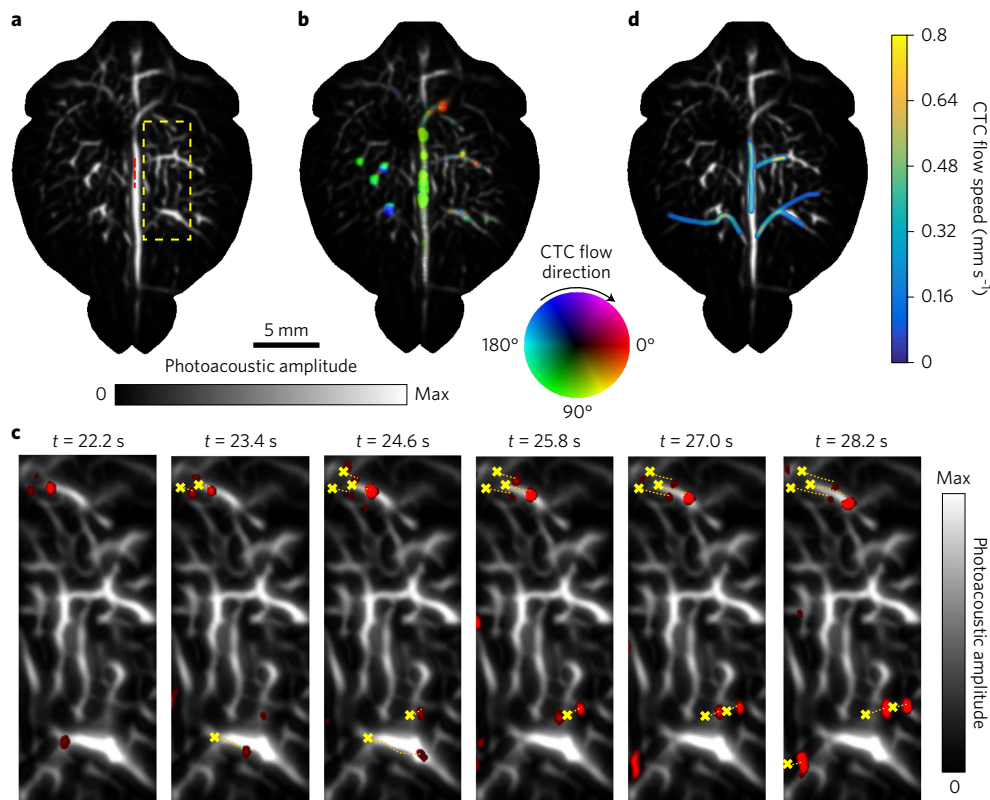
Figure 5 | Label-free tracking of CTCs in the mouse brain *in vivo*. a, Baseline cortical vasculature before the injection of melanoma cancer cells, under 680 nm excitation (Supplementary Video 11). **b**, Photoacoustic imaging of the mouse cortex after injection of melanoma cancer cells, where the colours represent the flow direction of CTCs. Flow speed is radially encoded in the colour disk by hue saturation (a greater radius indicates a faster flow speed). **c**, CTC flow over time, where red highlights the moving cancer cells in the current frame, yellow crosses show their initial positions, and orange dashed lines represent the flowing traces. **d**, Flow speed distribution of CTCs in segmented cortical vessels.

of each pixel along the red dashed line in Fig. 5a, and plotted the signals (Supplementary Fig. 17a) as an image in the space–time domain. By taking the 2D Fourier transformation of this image, we mapped lines with the same slope in the space–time domain onto a single line in the spatiotemporal frequency domain (Supplementary Fig. 17b), simplifying the calculation of the flow speed and providing better accuracy. The flow speed of the melanoma cells was computed by linear fitting to be 0.65 mm s⁻¹. Applying this method with a sliding window, we were able to visualize CTC flow speed distributions in multiple vessels of the brain (Fig. 5d). The flowing of melanoma cancer cells in both cortical arteries (Supplementary Fig. 18) and veins was visualized. We also observed occasionally ceased motion of melanoma cells, which might be a possible sign of the homing of metastasising cancer cells (Supplementary Fig. 19).

In addition, we imaged dye perfusion in both the mouse brain and the internal organs (Supplementary Figs 20–22 and Supplementary Video 12) after an intra-arterial injection of an NIR dye. We have therefore demonstrated SIP-PACT's potential for molecular imaging once the dye is functionalized.

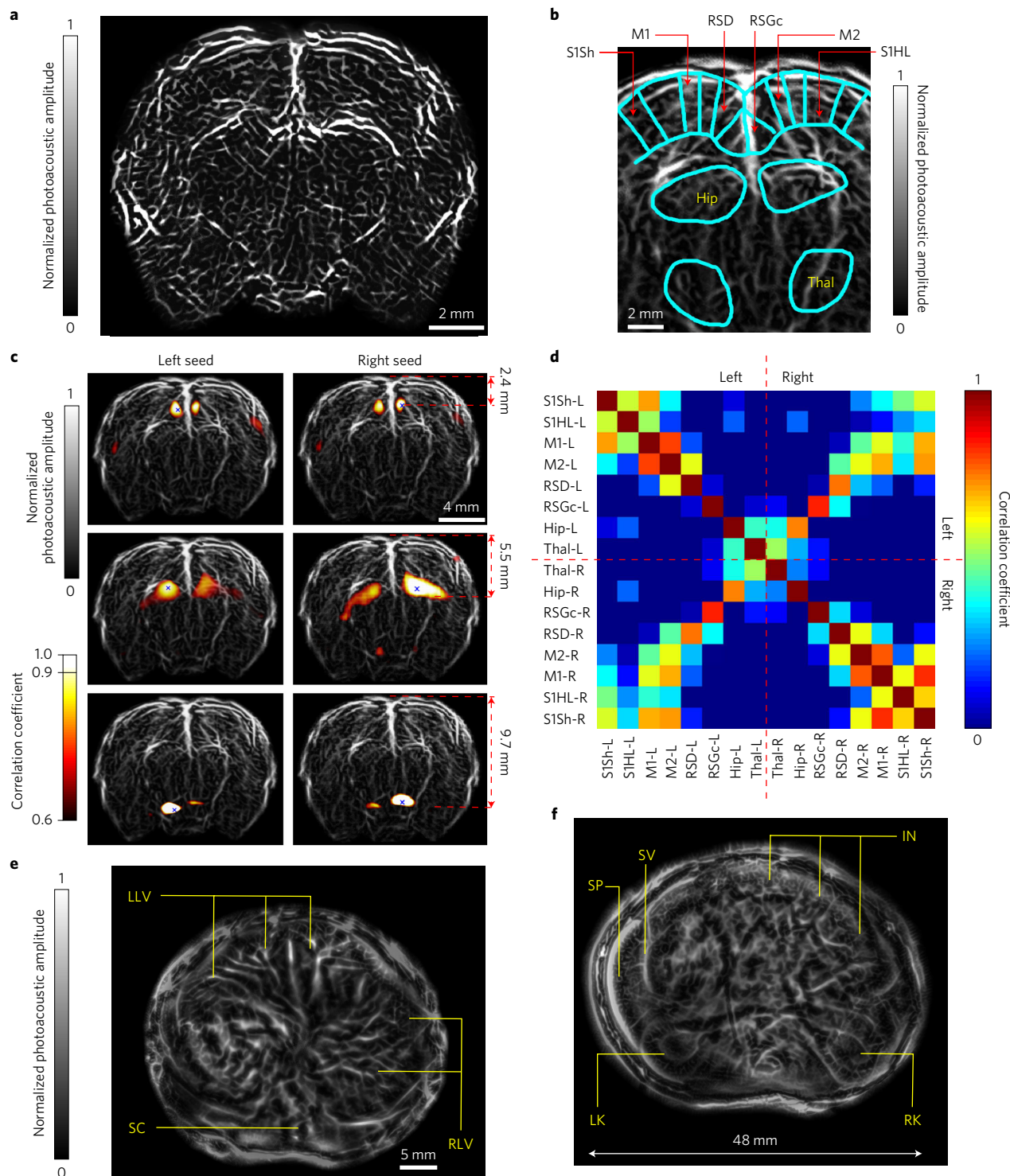**Deep imaging through rat whole brain and whole body.** Revealing how the human brain works is a great challenge that merits our every effort. It will not only illuminate the profound mysteries in science, but also provide the key to understanding and treating neurological diseases, such as Alzheimer's and Parkinson's. To date, most deep brain functional studies have been based on functional MRI (fMRI) or power Doppler ultrasound, and optically imaging through even a mouse brain (~6 mm in depth) with reasonable spatiotemporal resolution and contrast is still a hurdle. In this study, we used SIP-PACT to visualize a rat's whole brain.

As shown in Supplementary Fig. 23, the rat head was mounted vertically and the light was delivered obliquely to the rat cortex. A cranial window (see Methods) was opened to maximize the acoustic transmission. Taking advantage of the deep penetration of 1,064 nm light, the full-view acoustic coverage and high detection sensitivity of SIP-PACT (Supplementary Fig. 8), a coronal view of the rat whole brain (11 mm in depth) was produced with detailed vasculature (Fig. 6a).

The brain serves as the centre of the nervous system, dynamically coordinating responses through the functional network. The intrinsic functional connectivity across spatially separated brain regions can be measured through regionally correlated, spontaneous, low-frequency (0.01–0.1 Hz) fluctuations in BOLD signals with fMRI, particularly during resting state and task-free periods (resting state fMRI). Similar to fMRI, SIP-PACT can also globally monitor the brain haemodynamics with appropriate spatiotemporal resolution and penetration. To detect the functional connectivity, we measured and compared the spontaneous haemodynamic responses between contralateral regions of the rat brain. We measured the functional connectivity of the rat whole brain in the coronal plane (~bregma −2.16 mm), where we identified 16 functional regions (labelled in Fig. 6b) and computed the correlation coefficients of every pair (see Methods). We also employed a seed-based method (see Methods) to study the functional connectivity (Fig. 6c; Supplementary Fig. 24). The results (Fig. 6d) show clear correlation between corresponding regions across the left and right hemispheres, as well as correlation between neighbouring regions in the neocortex. These findings are consistent with previous research on both fMRI and power Doppler ultrasound[42,43]. Most interestingly, we identified the left–right correlation between the deep thalamus regions (9.7 mm in depth, Fig. 6c,

bottom row), which, to the best of our knowledge, has not been demonstrated at this spatial resolution. Our functional connectivity observation demonstrates the potential of SIP-PACT as a

high-resolution imaging tool for studying deep brain functions in rats, which was previously difficult to accomplish using optical contrast, and therefore underexplored.

Figure 6 | Deep imaging of rat whole-brain functions and whole-body anatomy. a, Rat whole-brain vasculature in the coronal plane. **b**, Segmentations of different functional regions of the brain. **c**, Seed-based functional connectivity analyses of RSGc (top row), the hippocampus (middle row) and the thalamus (bottom row) regions on both sides of the brain. **d**, Correlation matrix of the 16 functional regions labelled in **b**. Notice the correlation between left and right hemispheres, as well as the correlation across different regions in the neocortex. **e**,**f**, Cross-sectional images of a rat whole body (Supplementary Video 13). Hip, hippocampus; IN, intestine; LK, left kidney; LLV, left liver; M1, primary motor cortex; M2, secondary motor cortex; RK, right kidney; RLV, right liver; RSD, retrosplenial dysgranular cortex; RSGc, retrosplenial granular cortex; S1Sh, primary somatosensory–shoulder region; S1HL, primary somatosensory cortex–hindlimb region; SC, spinal cord; SP, spleen; SV, splenic vein; Thal, thalamus.

To further validate the deep penetration, an adult rat with a trunk (abdominal region) width of 48 mm was also imaged by SIP-PACT using side illumination (Fig. 1b). As shown in Fig. 6e,f, the internal organs, such as the left and right lobes of the liver, the kidneys, the spleen, the intestine and supply vessels, were clearly revealed (Supplementary Video 13).

Outlook

We have developed a SIP-PACT system that simultaneously integrates high spatiotemporal resolution, deep penetration, multiple contrasts, full-view fidelity and high detection sensitivity. SIP-PACT allows us to capture structural, functional, cellular and molecular small-animal whole-body images with 125 μm in-plane resolution within 50 μs per frame, using a single laser impulse per image. Panoramic acoustic detection provides the best in-plane coverage of ultrasound reception and eliminates partial-view artefacts related to the directive emission of photoacoustic waves. The substantially enhanced imaging performance enables SIP-PACT to complement existing modalities for small-animal whole-body imaging. The SIP-PACT system offers a number of whole-body imaging capabilities (Supplementary Table 1). It non-invasively images the mouse anatomy in real time, showing clearly resolved sub-organ vasculature and structures. Such a capability can be used for the direct diagnosis of pathological changes in internal organs. As a result, our technology opens a new window for medical researchers to test drugs and monitor longitudinal therapy, without the harm from ionising radiation associated with X-ray CT, PET or SPECT. Aortic pulse wave measurement and analysis have been widely used to study cardiovascular diseases in both clinical and preclinical research[26,27]. With a frame rate of 50 Hz, SIP-PACT reveals whole-body cardiac related dynamics and selectively maps the whole-body arterial network in mice. Relatively steady phase delays between arteries within internal organs can also be computed, which indicate changes in the cross-sectional areas resulting from pulse wave propagation through the arterial network. Thus, the capability of mapping the arterial network and the relative phase delay distribution within each cross-section enables SIP-PACT to be a potential non-invasive tool for the direct diagnosis of chronic coronary artery disease and chronic renal vascular disease. Evaluation of the haemodynamic response to oxygen challenges and the resulting changes in the blood oxygen level in the brain and body provides an effective means to access neural activity and whole-body metabolism. Leveraging the absorption spectral difference between oxyhaemoglobin and deoxyhaemoglobin, SIP-PACT achieves functional imaging in both the brain and the trunk, which enables applications, such as monitoring haemodynamic-related metabolic activities across internal organs during chemotherapy. We have shown that SIP-PACT has the ability to track unlabelled circulating melanoma cancer cells *in vivo* in the mouse brain. This capability might provide new insights into metastasis research, which can potentially be used to better tailor cancer therapies in the future. SIP-PACT also revealed detailed structures and vasculature in the whole cross-section of a rat trunk (48 mm in width) *in vivo*, which demonstrated a thickness potentially applicable to imaging human extremities or early birth neonates. In addition, a larger FOV and deeper acoustic penetration can be achieved by reducing the central frequency of the transducers to 1–2 MHz, which scales SIP-PACT up for human breast imaging. We envision potential applications of SIP-PACT in clinical translation and practice.

Photoacoustic imaging has already demonstrated its capability of functional brain imaging in rodents with exquisite sensitivity and high resolution at depths beyond the optical diffusion limit[16,44,45]. SIP-PACT has further extended the functional brain imaging depth to the rat whole brain (~10 mm in depth). An optical contrast and spatiotemporal resolution as fine as SIP-PACT provides has not previously been demonstrated. However, to reach the ultimate

goal of imaging single neuron action potentials at the whole-brain level, great efforts are needed to further improve the spatiotemporal resolution, sensitivity and voltage-sensitive photoacoustic contrast agents.

Methods

System construction and laser configuration. For SIP-PACT, we employed a 512-element full-ring ultrasonic transducer array (Imasonic Inc.; 50 mm ring radius; 5 MHz central frequency; more than 90% one-way bandwidth; Supplementary Fig. 1) for 2D panoramic acoustic detection. Each element has a cylindrical focus (0.2 NA; 20 mm element elevation size; 0.61 mm pitch; 0.1 mm inter-element spacing). A lab-made 512-channel preamplifier (26 dB gain) was directly connected to the ultrasonic transducer array housing, with minimized connection cable length to reduce cable noise. The preamplified photoacoustic signals were digitized using a 512-channel data acquisition system (four SonixDAQs, Ultrasonix Medical ULC; 128 channels each; 40 MHz sampling rate; 12 bit dynamic range) with programmable amplification up to 51 dB. The digitized radio frequency data were first stored in the onboard buffer, then transferred to a computer through universal serial bus 2.0.

For whole-body imaging illumination, a 1,064 nm laser beam (DLS9050, Continuum; 50 Hz pulse repetition rate; 5–9 ns pulse width) or a 720 nm laser beam (LS-2145-LT-150, Symphotic Tii; 20 Hz pulse repetition rate; 12 ns pulse width) was first homogenized and expanded by an engineered diffuser (EDC-10-A-1r, RPC Photonics), then passed through a conical lens (AX-FS-1-140-0, Del Mar Photonics) to form a ring-shaped light pattern, and refocused by a lab-made optical condenser. The incident light formed a ring pattern on the trunk of the mouse, with the illuminated area located within the transducer's elevational focal zone. For brain imaging illumination, the excitation beam was uniformly shined on the cortex after passing through the engineered diffuser. The laser fluence (8 mJ cm^{-2}) at 630 nm, 680 nm and 720 nm was within the American National Standards Institute (ANSI) safety limits for laser exposure (20 mJ cm^{-2} at 630 nm and 680 nm, and 40 mJ cm^{-2} at 720 nm, at a 10 Hz pulse repetition rate). The laser fluence in mouse and rat brain imaging, and in mouse trunk imaging, was approximately 18 mJ cm^{-2} at 1,064 nm, with a 50 Hz pulse repetition rate, which is below the ANSI safety limit (at 1,064 nm: 100 mJ cm^{-2} at a 10 Hz pulse repetition rate, or 1 W cm^{-2}). During the rat trunk imaging, the excitation fluence was approximately 38 mJ cm^{-2} at 1,064 nm, with a 50 Hz pulse repetition rate, which is above the ANSI limit. The rats were monitored periodically after imaging, and no skin damage was found.

For two-wavelength imaging, such as in the brain sO$_2$ mapping experiment, two lasers were synchronized by a control card (sbRIO-9626, National Instruments). The Q-switch trigger of each laser was set at a fixed delay of 50 μs, thus one laser fired 50 μs later than the other. Since the pulses at each of the two wavelengths were delayed by only 50 μs, during which time the object was relatively stationary in terms of most biological activities, we call the illumination essentially simultaneous.

Animal preparation. All experimental procedures were carried out in conformity with laboratory animal protocols approved by the Animal Studies Committee at Washington University in St. Louis. Adult, three- to four-month-old Swiss Webster mice (Hsd:ND4, Swiss Webster, Harlan Co.; 20–30 g body weight) were used for *in vivo* functional brain and CTC imaging. Adult, two- to three-month-old Sprague Dawley rats (Hsd:Sprague Dawley SD, Harlan Co.; 170–200 g body weight) were used for *in vivo* rat brain imaging of function connectivity. Adult eight- to ten-week-old nude mice (Hsd:Athymic Nude-FoxlNU, Harlan; 20–30 g body weight) were used for *in vivo* mouse trunk imaging. Adult two-month-old nude rats (Hsd:Athymic Nude-Foxn1rnu (rnu/rnu), Harlan; 150–160 g body weight) were used for *in vivo* rat trunk imaging. Throughout the experiment, the mouse was maintained under anaesthesia with 1.5% vapourized isoflurane. Before functional brain and CTC imaging experiments, the hair of the mouse was first removed using clippers and depilatory cream. The mouse was then secured to a lab-made imaging platform, and the cortical surface was positioned flat and lined up with the transducer array's focal plane. During the whole-body imaging experiments (Supplementary Fig. 4), the mouse or rat's fore and hind legs were respectively taped to the top and bottom parts of the lab-made holder, which held the animal upright during imaging. The top of the holder was an aluminium tube affixed to the animal's nose and mouth, and the bottom was an aluminium cylinder attached to a permanent magnet base. The magnet base securely held the animal holder to the scanning stage for elevational scanning. It takes about 12 s to scan the whole trunk to acquire a volume containing 600 cross-sectional images. The animal's trunk was immersed in water, and its body temperature was maintained at around 30 °C by circulating the water through a heating bath outside the tank.

Before functional rat brain imaging experiments, a craniotomy was conducted by the Hope Center Animal Surgery Core at Washington University. Under isoflurane anaesthesia, the rat was placed in a stereotaxic apparatus. After being shaved and swabbed, the scalp was incised and retracted. The parietal bone was then removed using a fine drill bit, with frequent irrigation and swabbing with cold, sterile phosphate-buffered saline. Finally, the bone flap was removed over

an area of approximately 0.5 cm × 0.9 cm to expose the brain (parietal lobes). The rat head was mounted vertically and the light was obliquely illuminated onto the rat cortex (Supplementary Fig. 23). After locating the proper imaging plane (coronal view) of the rat brain, the isoflurane level was changed to 0.5% from 1.5%. After 40 min, we started the measurement of functional connectivity. Each functional connectivity measurement took 10 min, with a 2 Hz frame rate at 1,064 nm illumination.

Both the melanoma cancer cells and NIR dye were injected through the carotid artery. Ligatures of the external and the common carotid artery[46] were constructed by the Hope Center Animal Surgery Core at Washington University in St. Louis. For melanoma cancer cell imaging, we injected 100 μL of a cell suspension containing 1×10^{6} B16 cells. For dye perfusion imaging, we injected 100 μL of NIR dye (FHI 104422P, Fabricolor Holding International LLC) solution with a 0.5% mass concentration.

Half-time, dual-speed-of-sound photoacoustic reconstruction. We used the half-time UBP algorithm[47,48] to reconstruct all images in this work. Conventional half-time UBP assumes a uniform speed of sound (SOS) to calculate the photoacoustic signal delay necessary for the reconstruction. In real applications, however, the heterogeneous acoustic properties of the substances within the elevational focal plane render the uniform SOS assumption problematic. Consequently, the resulting images always suffer from artefacts that cannot be removed or alleviated by image processing techniques, such as deconvolution. In the case of whole-body imaging, at a given elevational position, breakdown of the uniform SOS assumption mainly results from the dramatic acoustic property difference between the biological tissue and the surrounding fluid (in our case, water), whereas the SOS differences among different tissue types cause only second-order effects. For example, at room temperature, the SOS of water, the liver and the kidney are 1,480 m s⁻¹, 1,590 m s⁻¹ and 1,570 m s⁻¹, respectively[25].

We numerically simulated the problem in 2D using a circular numerical phantom with a radius of 13 mm and a uniform SOS of 1,520 m s⁻¹. The phantom was surrounded by water with an SOS of 1,480 m s⁻¹, and the whole region was bounded by a ring-shaped detector array with a radius of 50 mm. The phantom and the ring array were located concentrically, as shown in Supplementary Fig. 2a. Within the phantom, an optical absorption pattern representing a leaf skeleton was used (Supplementary Fig. 2b). We used the k-Wave toolbox to generate photoacoustic data[49], and reconstructed images from the data using half-time UBP with single and dual SOS. We compared the images reconstructed using a single uniform SOS (Supplementary Fig. 2c) and the correct (Supplementary Fig. 2d) dual-SOS map. Clearly, a single SOS reconstruction introduces splitting or fringing artefacts in the image (Supplementary Fig. 2c, inset zoomed-in view).

To date, many methods have been developed to solve the problem caused by SOS heterogeneity. These methods either rely on iterative SOS corrections[28] or use additional hardware and software to measure the SOS map[50]. Both approaches dramatically increase the complexity of signal demodulation and image reconstruction. Here, to improve the image quality, we used a method that imposes no additional computational cost. The key is to correct the first-order errors only. In doing so, we segment the entire region into two zones: a tissue zone and a water zone. We assume that the SOS is uniform within each zone, but is different across the zones. To further simplify the problem, we make the following two assumptions. First, the cross-section of the mouse body is approximated by an ellipse characterized by its centre position (x_0, y_0) and the lengths of its major and minor radii (R_x, R_y). Second, refraction at the boundary of the two zones is neglected. In other words, rays travel straight from the field point (x_s, y_s) to a detector (x_d, y_d). The second assumption is sufficiently accurate, according to a simple geometrical analysis[25]. Using these assumptions, we can calculate the sound propagation delay between any source–detector pairs given the SOS in the body (v_1) and water (v_2) (Supplementary Fig. 3a). It should be noted that if a series of images are taken at, or close to, a fixed elevational position, the delay map is calculated only once before reconstruction. Subsequently, we can use the delay map generated by the dual-speed assumption to reconstruct images with no additional computational cost. In Supplementary Fig. 3b, we illustrate the gross localisation error produced by the single-speed assumption. In the calculation, we assumed that $R_x = R_y = 10$ mm, $x_0 = y_0 = 0$, and $v_1 = 1,570$ m s⁻¹, $v_2 = 1,506$ m s⁻¹, and $R_d = 50$ mm. The photoacoustic signal generated by a point source, located at the position labelled by a red star in Supplementary Fig. 3b, was back-projected along the direction piercing the source and the detector. The reconstructed position of the point source, according to the single-speed assumption, scatters around the correct position, depending on the azimuthal angle of the transducer. A splitting as large as 0.4 mm is observed. In Supplementary Fig. 3c,d, we compare the images of the liver region of a mouse reconstructed using half-time single-speed (Supplementary Fig. 3c) and half-time dual-speed (Supplementary Fig. 3d) UBP approaches. Supplementary Fig. 3c shows many artefacts, including the horseshoe-shaped features on the body surface (which are shown as blood vessels perpendicular to the image plane in Supplementary Fig. 3d), and splitting of the vasculature in the upper-left and lower-right regions of the body. These artefacts are completely removed by the dual-speed reconstruction, as shown in Supplementary Fig. 3d. The acquired data were reconstructed offline using the half-time dual-speed-of-sound universal

back-projection method, and it takes approximately 0.1 s to reconstruct one frame with 400 × 400 pixels using intel i7 central processing unit, which can be further accelerated by graphics processing unit parallel computing.

Methods for whole-body image contrast enhancement. To produce the high-contrast small animal whole-body anatomical images illustrated in this work, we first applied a set of Hessian-based Frangi vesselness filters[51] at different scales to the reconstructed 2D images. Next, all of the filtered images were averaged to produce the output images. These two steps form our multiscale vessel enhancing filtering. We applied this filtering scheme to both the negative and positive components of the input image, to account for its bipolar nature (for instance, both the most negative and most positive values represent large optical absorption). The results from both the negative and positive components were then added to form the final image. The filter scales used in all of the enhanced images in this work were 0.05, 0.10, 0.15, 0.20, 0.50, 0.75, 1.00 and 1.25 mm. These were chosen empirically to cover the range of one half to ten times the quantified resolution (0.125 mm). As shown in Supplementary Fig. 5, the anatomical structures in both the original bipolar images and enhanced unipolar images match well with each other.

Since this contrast enhancement technique is nonlinear, we are aware that it would induce inaccuracy if its results were used for quantitative analyses. Therefore, all of the functional and quantitative calculations in this work were based on the raw, bipolar reconstructed images without the contrast-enhancing filtering.

Illumination wavelength selection. The molar optical absorption of deoxyhaemoglobin is much higher than that of oxyhaemoglobin within the wavelength range of 600–800 nm (Supplementary Fig. 15a). Thus, when the excitation wavelength is within this range, the photoacoustic signal is more sensitive to the change of deoxyhaemoglobin concentration (Supplementary Fig. 15b). We chose 720 nm for whole-body functional imaging to balance the penetration depth and deoxyhaemoglobin sensitivity.

The optical absorption of melanosome decreases slowly with an increase in wavelength, and the optical absorption of haemoglobin is relatively weak within the far-red and NIR regions. The optical absorption ratio between melanosome and whole blood (at 85% sO₂) peaks at around 680 nm (Supplementary Fig. 16a), and thus an excitation wavelength of 680 nm (Q-Smart 850, Quantel; 10 Hz pulse repetition rate; 6 ns pulse width; and basiScan-M/280, Newport) was used for imaging circulating melanoma cancer cells.

Fourier domain analysis of whole-body dynamics. To demonstrate the motion in the thoracic cavity, the photoacoustic signals along the lines indicated in Fig. 3a were extracted and the primary peaks in each frame were tracked. For each line examined, the peak's position formed a time trace and was transformed into the temporal frequency domain, where the respiratory frequency components and/or the heartbeat frequency components were visualized.

To map the arterial network, Fourier transform was performed on the time trace from each pixel. The amplitude at the heartbeat frequency was extracted to form the artery map.

To analyse the phase delay across different arteries, we examined neighbouring patches of the selected vertically distributed arteries, segmented the arteries at each frame by thresholding, and computed the area values. The changes in the cross-sectional areas were then calculated and filtered with a high-pass filter to remove low-frequency interferences. The zero-phase digital filtering technique was used to avoid changing the phase information, and the cutoff frequency was set at the halfway point between the respiratory frequency's second harmonic and the heartbeat frequency. For demonstration purposes, the changes for different arteries were normalized to 0 and 1, according to their minimum and maximum values, which did not alter phase information.

Functional imaging of brain and whole-body oxygenation. In this study, the oxygen challenge protocol was as follows. A mixture of 95% oxygen and 5% nitrogen was initially used for 3 min, then the mixture was changed to 5% oxygen and 95% nitrogen for 3 min (4.5 min for whole-body oxygen challenge) and finally changed back to the initial concentration to end the challenge.

To generate Supplementary Video 9, we took 4,000 images at 10 Hz, using the essentially simultaneous illumination scheme (Fig. 1a). We used 1,064 nm (DLS9050, Continuum; 50 Hz pulse repetition rate; 5–9 ns pulse width) and 630 nm (Q-Smart 850, Quantel; 10 Hz pulse repetition rate; 6 ns pulse width; and basiScan-M/280, Newport) for illumination and the following equations for the calculation of sO₂:

$$\begin{bmatrix} C_{HbO_2} \\ C_{Hb} \end{bmatrix} = \begin{bmatrix} \varepsilon_{HbO_2} & \varepsilon_{Hb} \\ \varepsilon_{HbO_2} & \varepsilon_{Hb} \end{bmatrix}^{-1} \begin{bmatrix} PA_{630}/F_{630} \\ PA_{1,064}/F_{1,064} \end{bmatrix} \qquad sO_2 = \frac{C_{HbO_2}}{C_{HbO_2} + C_{Hb}}$$

In the above equations, PA represents photoacoustic amplitude, F is the optical fluence at the blood vessel being imaged, ε represents the molar extinction coefficient, C is concentration, Hb is deoxyhaemoglobin and HbO₂ is oxyhaemoglobin. To estimate PA/F, we normalized all channel data using the signal generated at

the transducer's surface. We divided the original 4,000 frames of raw data into 160 bins and averaged within each bin on a per channel basis. The data cube was subsequently averaged along the third dimension (time) with a window size of five. The reconstructed images were smoothed using a Hessian filter, and we segmented several branches of vessels to display the calculated sO_2 in colour. The average sO_2 value of the central vein was plotted as a function of time to show the dynamic relative change.

To generate the images shown in Fig. 4e, we averaged the first 1,000 frames (corresponding to the first 50 s of the experiment) of the whole-body functional images as the baseline image. Then we averaged 2,500 frames (corresponding to the time from 180 s to 305 s) during the oxygen challenge as the challenge signal image. A relative signal change image can be computed between the baseline image and the challenge signal image. A disk filter (with a size of 5 pixels, from the Matlab Image Processing Toolbox) was applied to the relative signal change image and then overlaid on the anatomy image.

Supplementary Video 10 was created with a method similar to that used in Fig. 4e. We calculated the baseline from the average of the first 1000 frames (50 s), and used a 375 frame (18.75 s) moving window to monitor the dynamic changes thereafter. The overlay images were also smoothed with a 5 pixel (0.25 mm) disk filter.

To generate the comparison shown in Fig. 4f, we randomly picked 50 pixels within each respective anatomical region in Fig. 4e. Their pixel values at randomly selected frames within the baseline (before the oxygen challenge procedure) and plateau (during the oxygen challenge procedure) time windows were extracted for statistical analysis. Because each pixel had a baseline value and a plateau value, a paired Student's t-test was employed to compute the P-value. Due to the difficulties of directly comparing signal levels across animals, the statistical analysis only considered samples from the same animal. Additional results from the other two animals can be found in Supplementary Fig. 15c,d.

Flowing of melanoma cancer cells. We estimated the local motion vectors from consecutive frames in Supplementary Video 11 using a dense optical flow-based algorithm[52], and plotted their amplitude and direction with brightness and colour (Fig. 5b).

The vessels that contained flowing melanoma cancer cells were first manually identified from the video (Supplementary Video 11). Time traces at points along these vessels were then extracted, forming images in which one dimension was the distance along the vessels (x) and the other dimension was the elapsed time (t). Taking a 2D Fourier transform of these images mapped lines with the same angle in the x–t space onto a single line passing the origin in the spatiotemporal frequency domain. After removing the two direct current components and thresholding at 10% of the maximum amplitude, we applied linear fitting to the transformed images to estimate an overall flow speed. For a long vessel, where we believed a speed distribution should be present, we used a heuristically determined 1.5 mm sliding window and applied the aforementioned method within the window to calculate the flow speed changes along the vessel. Akin to all windowed frequency analyses, tuning the window size allowed us to balance between flow speed quantification accuracy and the spatial resolution of the speed map.

Functional connectivity of the rat brain. In order to measure the functional connectivity of the rat brain, we adopted a data analysis method previously reported[53]. Briefly, the images were first filtered using a 5 pixel disk filter to reduce motion noises due to respiration. A region of interest (ROI) in the visible brain area was then identified manually. A second-order Butterworth bandpass filter (0.01 Hz to 0.1 Hz) was subsequently applied to all temporal sequences. Global signal regression was performed based on the time sequences of all pixels within the ROI. In seed-based functional connectivity studies, we picked a seed in the image and computed the correlation coefficients between all pixels in the ROI and the seed (Fig. 6c). In functional region-based functional connectivity analyses, we identified the functional regions, averaged the signals from pixels within a region, and computed correlation coefficients between regions to form a connectivity network image (Fig. 6d).

Whole-body rat image processing. The full-ring transducer array with 512 elements can sample the object spatially well within a FOV of around 16.3 mm in diameter, as determined by the equation below:

$$N\frac{\lambda}{2} = \pi D$$

where $N = 512$ is the number of elements, $\lambda = 200\,\mu m$ is the wavelength corresponding to the high cut-off frequency of the transducer and D is the diameter of the FOV. If the FOV is increased, the peripheral region becomes sparsely sampled. To address the reconstructed artefacts induced by the sparse sampling, we applied the following method.

The raw ultrasound channel data were first filtered using three low-pass filters with cutoff frequencies at 10 MHz, 7.5 MHz and 5 MHz, respectively, corresponding to FOVs with diameters of 25 mm, 37.5 mm and 50 mm. The three filtered channel data sets were then used to reconstruct three images. One disk-shaped mask and two doughnut-shaped masks selecting these FOVs were created and blurred with a 5 pixel standard deviation Gaussian filter. The blurred

mask images were then multiplied with the three reconstructed images, and the resultant images were added together to produce the final reconstructed image.

SIP-PACT has a high dynamic range due to its low noise figure, which is enabled by the preamplifiers. This advantage helps us to mitigate the problem of light attenuation by the relatively thick rat trunk tissue, enabling accurate detection of small signals in deep tissue. To better represent these images, we employed an adaptive gain compensation method, which is similar to the time gain compensation widely used in ultrasound imaging. The image was segmented into 50 concentric rings from the centre of the object to the farthest edge of the object. Pixel values from within each ring and above two times the noise level were averaged as the baseline signal level of the ring. Pixels within each ring were then normalized to the baseline signal level of the ring. The adaptive gain compensation method notably enhanced the overall visibility of small features at depths, while maintaining the local contrast-to-noise ratio.

Reproducibility. The experiments were not randomized. The investigators were not blinded to allocation during experiments and outcome assessment. No sample size estimation was performed to ensure adequate power to detect a prespecified effect size.

Code availability. The reconstruction algorithm and data processing methods are described in detail in the Methods. We have opted not to make the data acquisition, image reconstruction and processing code available because the code is proprietary and used for other projects.

Data availability. The authors declare that all data supporting the findings of this study are available within the paper and its Supplementary Information.

References

1. Baker, M. Whole-animal imaging: the whole picture. *Nature* **463**, 977–980 (2010).
2. Zanzonico, P. in *Small Animal Imaging: Basics and Practical Guide* (eds Kiessling, F. & Pichler, J. B.) 3–16 (Springer, 2011).
3. Ntziachristos, V. Going deeper than microscopy: the optical imaging frontier in biology. *Nat. Methods* **7**, 603–614 (2010).
4. Jun, X. & Wang, L. V. Small-animal whole-body photoacoustic tomography: a review. *IEEE Trans. Biomed. Eng.* **61**, 1380–1389 (2014).
5. Wu, D. & Zhang, J. *In vivo* mapping of macroscopic neuronal projections in the mouse hippocampus using high-resolution diffusion MRI. *Neuroimage* **125**, 84–93 (2016).
6. Alomair, O. I., Brereton, I. M., Smith, M. T., Galloway, G. J. & Kurniawan, N. D. *In vivo* high angular resolution diffusion-weighted imaging of mouse brain at 16.4 Tesla. *PLoS ONE* **10**, e0130133 (2015).
7. Schambach, S. J., Bag, S., Schilling, L., Groden, C. & Brockmann, M. A. Application of micro-CT in small animal imaging. *Methods* **50**, 2–13 (2010).
8. Brenner, D. J. & Hall, E. J. Computed tomography—an increasing source of radiation exposure. *N. Engl. J. Med.* **357**, 2277–2284 (2007).
9. Greco, A. *et al.* Ultrasound biomicroscopy in small animal research: applications in molecular and preclinical imaging. *J. Biomed. Biotechnol.* **2012**, 519238 (2012).
10. Kim, T. *et al.* White-light diffraction tomography of unlabelled live cells. *Nat. Photon.* **8**, 256–263 (2014).
11. Horton, N. G. *et al. In vivo* three-photon microscopy of subcortical structures within an intact mouse brain. *Nat. Photon.* **7**, 205–209 (2013).
12. Zhang, F. *et al.* Multimodal fast optical interrogation of neural circuitry. *Nature* **446**, 633–639 (2007).
13. Darne, C., Lu, Y. & Sevick-Muraca, E. M. Small animal fluorescence and bioluminescence tomography: a review of approaches, algorithms and technology update. *Phys. Med. Biol.* **59**, R1–R64 (2014).
14. Razansky, D. *et al.* Multispectral opto-acoustic tomography of deep-seated fluorescent proteins *in vivo*. *Nat. Photon.* **3**, 412–417 (2009).
15. Wang, L. H. V. & Hu, S. Photoacoustic tomography: *in vivo* imaging from organelles to organs. *Science* **335**, 1458–1462 (2012).
16. Yao, J. *et al.* High-speed label-free functional photoacoustic microscopy of mouse brain in action. *Nat. Methods* **12**, 407–410 (2015).
17. Jathoul, A. P. *et al.* Deep *in vivo* photoacoustic imaging of mammalian tissues using a tyrosinase-based genetic reporter. *Nat. Photon.* **9**, 239–246 (2015).
18. Yao, J. *et al.* Multiscale photoacoustic tomography using reversibly switchable bacterial phytochrome as a near-infrared photochromic probe. *Nat. Methods* **13**, 67–73 (2016).
19. Brecht, H.-P. *et al.* Whole-body three-dimensional optoacoustic tomography system for small animals. *J. Biomed. Opt.* **14**, 064007 (2009).
20. Taruttis, A., Morscher, S., Burton, N. C., Razansky, D. & Ntziachristos, V. Fast multispectral optoacoustic tomography (MSOT) for dynamic imaging of pharmacokinetics and biodistribution in multiple organs. *PLoS ONE* **7**, e30491 (2012).

21. Merčep, E., Burton, N. C., Claussen, J. & Razansky, D. Whole-body live mouse imaging by hybrid reflection-mode ultrasound and optoacoustic tomography. *Opt. Lett.* **40,** 4643–4646 (2015).

22. Razansky, D., Buehler, A. & Ntziachristos, V. Volumetric real-time multispectral optoacoustic tomography of biomarkers. *Nat. Protoc.* **6,** 1121–1129 (2011).

23. Luis Dean-Ben, X. & Razansky, D. Adding fifth dimension to optoacoustic imaging: volumetric time-resolved spectrally enriched tomography. *Light Sci. Appl.* **3,** e137 (2014).

24. Tang, J., Coleman, J. E., Dai, X. & Jiang, H. Wearable 3-D photoacoustic tomography for functional brain imaging in behaving rats. *Sci. Rep.* **6,** 25470 (2016).

25. Yuan, X. & Wang, L. V. Effects of acoustic heterogeneity in breast thermoacoustic tomography. *IEEE Trans. Ultrason. Ferroelectr. Freq. Control* **50,** 1134–1146 (2003).

26. Cohn, J. N. *et al.* Noninvasive pulse-wave analysis for the early detection of vascular-disease. *Hypertension* **26,** 503–508 (1995).

27. Kis, E. *et al.* Pulse wave velocity in end-stage renal disease: influence of age and body dimensions. *Pediatr. Res.* **63,** 95–98 (2008).

28. Stein, E. W., Maslov, K. & Wang, L. V. Noninvasive, *in vivo* imaging of blood-oxygenation dynamics within the mouse brain using photoacoustic microscopy. *J. Biomed. Opt.* **14,** 020502 (2009).

29. Xia, J. *et al.* Calibration-free quantification of absolute oxygen saturation based on the dynamics of photoacoustic signals. *Opt. Lett.* **38,** 2800–2803 (2013).

30. Raichle, M. E. Behind the scenes of functional brain imaging: a historical and physiological perspective. *Proc. Natl Acad. Sci. USA* **95,** 765–772 (1998).

31. Ogawa, S., Lee, T.-M., Kay, A. R. & Tank, D. W. Brain magnetic resonance imaging with contrast dependent on blood oxygenation. *Proc. Natl Acad. Sci. USA* **87,** 9868–9872 (1990).

32. Roberts, M. B. V. in *Biology: A Functional Approach* 4th edn, 243–249 (Thomas Nelson and Sons, 1986).

33. Joiner, J. T. in *NOAA Diving Manual: Diving For Science And Technology* 4th edn, 1–36 (Best Publishing Company, 2001).

34. Karimova, A. & Pinsky, J. D. The endothelial response to oxygen deprivation: biology and clinical implications. *Intensive Care Med.* **27,** 19–31 (2001).

35. Piantadosi, C. A. in *The Biology of Human Survival: Life and Death in Extreme Environments* 129–139 (Oxford Univ. Press, 2003).

36. Miura, G. Cancer tumor imaging: catch me if you can. *Nat. Chem. Biol.* **10,** 485–485 (2014).

37. Nagrath, S. *et al.* Isolation of rare circulating tumour cells in cancer patients by microchip technology. *Nature* **450,** 1235–1239 (2007).

38. Kienast, Y. *et al.* Real-time imaging reveals the single steps of brain metastasis formation. *Nat. Med.* **16,** 116–122 (2010).

39. Siegel, R. L., Miller, K. D. & Jemal, A. Cancer statistics, 2016. *CA Cancer J. Clin.* **66,** 7–30 (2016).

40. Srinivasan, V. J. *et al.* Quantitative cerebral blood flow with optical coherence tomography. *Opt. Express* **18,** 2477–2494 (2010).

41. Cox, S. B., Woolsey, T. A. & Rovainen, C. M. Localized dynamic changes in cortical blood flow with whisker stimulation corresponds to matched vascular and neuronal architecture of rat barrels. *J. Cereb. Blood Flow Metab.* **13,** 899–913 (1993).

42. Jonckers, E., Van Audekerke, J., De Visscher, G., Van der Linden, A. & Verhoye, M. Functional connectivity fMRI of the rodent brain: comparison of functional connectivity networks in rat and mouse. *PLoS ONE* **6,** e18876 (2011).

43. Osmanski, B.-F., Pezet, S., Ricobaraza, A., Lenkei, Z. & Tanter, M. Functional ultrasound imaging of intrinsic connectivity in the living rat brain with high spatiotemporal resolution. *Nat. Commun.* **5,** 5023 (2014).

44. Dean-Ben, X. L. *et al.* Functional optoacoustic neuro-tomography for scalable whole-brain monitoring of calcium indicators. *Light Sci. Appl.* **5,** e16201 (2016).

45. Gottschalk, S., Fehm, T. F., Deán-Ben, X. L. & Razansky, D. Noninvasive real-time visualization of multiple cerebral hemodynamic parameters in whole mouse brains using five-dimensional optoacoustic tomography. *J. Cereb. Blood Flow Metab.* **35,** 531–535 (2015).

46. Schackert, G., Price, J. E., Bucana, C. D. & Fidler, I. J. Unique patterns of brain metastasis produced by different human carcinomas in athymic nude mice. *Int. J. Cancer* **44,** 892–897 (1989).

47. Anastasio, M. A. *et al.* Half-time image reconstruction in thermoacoustic tomography. *IEEE Trans. Med. Imaging* **24,** 199–210 (2005).

48. Xu, M. & Wang, L. V. Universal back-projection algorithm for photoacoustic computed tomography. *Phys. Rev. E* **71,** 016706 (2005).

49. Treeby, B. E. & Cox, B. T. K-Wave: MATLAB toolbox for the simulation and reconstruction of photoacoustic wave fields. *J. Biomed. Opt.* **15,** 021314 (2010).

50. Xia, J., Huang, C., Maslov, K., Anastasio, M. A. & Wang, L. V. Enhancement of photoacoustic tomography by ultrasonic computed tomography based on optical excitation of elements of a full-ring transducer array. *Opt. Lett.* **38,** 3140–3143 (2013).

51. Frangi, A. F., Niessen, W. J., Vincken, K. L. & Viergever, M. A. in *International Conference on Medical Image Computing and Computer-Assisted Intervention* (eds Wells, W. M., Colchester, A. & Delp, S.) 130–137 (Springer, 1998).

52. Farnebäck, G. in *Image Analysis* (eds Bigun, J. & Gustavsson, T.) 363–370 (Springer, 2003).

53. White, B. R. *et al.* Imaging of functional connectivity in the mouse brain. *PLoS ONE* **6,** e16322 (2011).

Author contributions

L.Li and L.V.W. conceived and designed the study. L.Li and L.Z. constructed the hardware system. L.Li, L.Z. and C.M. developed the software system and the reconstruction algorithm. L.W. and J.S. constructed the control program. K.M. and W.C. designed the preamplifiers. L.Li, C.M. and L.Lin performed the experiments. R.Z. cultured the B16 cells. L.Li, L.Z., C.M. and J.Y. analysed the data. L.V.W. supervised the study. All authors contributed to the writing of the manuscript.

Additional information

Supplementary information is available for this paper.

Reprints and permissions information is available at www.nature.com/reprints.

Correspondence and requests for materials should be addressed to L.V.W.

How to cite this article: Li, L. *et al.* Single-impulse panoramic photoacoustic computed tomography of small-animal whole-body dynamics at high spatiotemporal resolution. *Nat. Biomed. Eng.* **1,** 0071 (2017).

Publisher's note: Springer Nature remains neutral with regard to jurisdictional claims in published maps and institutional affiliations.

Competing interests

L.V.W. and K.M. have a financial interest in Microphotoacoustics, Inc.; however, Microphotoacoustics, Inc. did not support this work. The other authors declare no competing financial interests.